PCCP

Accepted Manuscript

ROYAL SOCIETY OF CHEMISTRY

www.rsc.org/pccp

Three-dimensional N, B-doped graphene aerogels as a synergistically enhanced metal-free catalyst for the oxygen reduction reaction

Congcong Xu,[a] Yan Su,[a] Dajun Liu,[a] Xingquan He*[a]

[a]*Department of Chemistry and Chemical Engineering, Changchun University of Science and Technology, Changchun 130022, P. R. China.*

* Corresponding author. Tel.+86-431-85583430

E-mail address:hexingquan@hotmail.com (Xingquan He);

Abstract

Here, a novel N, B-doped graphene aerogels, abbreviated as N, B-GAs, are obtained via a two-step approach and served as a metal-free catalyst for the oxygen reduction reaction (ORR). This two-step method involves a hydrothermal reaction and a pyrolysis procedure, guaranteeing the efficient insertion of heteroatoms. The resulting three-dimensional (3D) N, B-GAs exhibits an outstanding catalytic activity for the oxygen reduction reaction (ORR) comparable with Pt/C. In addition, the catalytic activity of the 3D N, B-GAs is obviously better than that of the nitrogen-doped graphene aerogels (N-GAs) or boron-doped graphene aerogels (B-GAs) in terms of the onset potential, half-wave potential and diffusion limiting current density. The superior catalytic reactivity arises from the synergistic coupling of the B and N dopants on the graphene domains.

Keywords: N, B-doped graphene aerogels; hydrothermal reaction; pyrolysis procedure; oxygen reduction reaction

1. Introduction

The past few decades have witnessed an astonishing growth in energy demand. Seeking economic, abundant and clean power sources has been the focus of plenty of efforts.[1] Fuel cells have been considered as potentially clean and high-efficient power sources for mobile and stationary applications because of their low operating temperature, environmentally-friendly nature, high energy density and high energy efficiency.[2-4] In this aspect, catalysts for the oxygen reduction reaction (ORR) are key components of fuel cells.[2] Pt and its alloys have long been regarded as the most efficient catalysts for the ORR. However, the limited natural reserves and high price

of Pt, together with the issues of instability and deactivation by CO poisoning and crossover effect, have restricted the large-scale application of fuel cells.[5] Therefore, enormous efforts have been devoted to seeking non-precious-metal[6-9] or even metal-free catalysts for the ORR.[10,11] Although extensive studies have been conducted in the search for non-precious catalysts, the results are far from satisfying because of the limited performance of the discovered catalysts and environmental hazards.[12]

Recently, much attention has been paid to the doping of heteroatoms into carbon matrices to modify the chemical and physical properties of the carbon materials.[13-17] In particular, graphene, a two-dimensional monolayer structure of sp^2-hybridized carbon, has become an attractive candidate for catalysis and energy applications due to its outstanding conductivity, high surface area and excellent mechanical properties, which provides an effective platform for fundamental investigations of the nature of metal-like reactivity in all carbon-based materials.[18] For catalytic applications, the engineering of pristine graphene by the substitution of some carbon atoms with heteroatoms, such as N, B, P, I and S, is an effective way to tailor its electron-donor properties and consequently enhance its catalytic activity.[9, 19-22] It is generally believed that co-doping with two elements, such as B and N, can generate a synergistic coupling effect between heteroatoms, which makes such dual-doped graphene catalysts much more catalytically active than singly doped graphene catalysts.[1, 12, 23] In addition, their atomic sizes would be acceptable for doping of the carbon lattice of graphene. In this regard, co-doping of graphene with two or more

selected heteroatoms is becoming one of the main trends in the tailoring of its chemical and physical properties for desired applications.

At present, the N, B-doped graphene has been achieved by diverse approaches such as chemical vapor deposition (CVD),[23-26] thermal annealing[1, 14, 27, 28] and solvothermal synthesis.[29] However, the aforementioned methods are effective only for obtaining single-doped graphene but not for co-doped graphene. For example, the pyrolysis method is effective for the synthesis of N- or B-doped graphene, but in the presence of both B and N atoms, it produced the covalent B–C–N bonding in graphene instead of B and N co-doped graphene.[1, 12, 28] Besides, this method also produced undesired by-products, such as hexagonal boron nitride, which is chemically inert and can reduce the activity of the catalyst. B and N co-doped graphene has proven to possess superior ORR activity due to its unique electronic structure with cooperativity between B and N.[12] Therefore, an efficient strategy that can be used for N and B co-doping of graphene is highly required.

In order to prepare desired N, B-doped samples, we propose a new, two-step synthesis strategy. In the first step, the hydrothermal reaction of graphite oxide (GO) with urea and chitosan was performed to produce the three-dimensional (3D) nitrogen-doped graphene aerogels, denoted as N-GAs. Subsequently, the N-GAs was mixed with boric acid and pyrolyzed in argon to produce N and B co-doped 3D graphene aerogels, abbreviated as N, B-GAs. The obtained N, B-GAs catalyst showed high catalytic activity, excellent methanol tolerance and good durability. Compared with other synthetic methods, our approach only requires common chemicals and

nontoxic precursors, is thus environmental friendly. The superior performance of our proposed N, B-GAs makes it a promising catalyst for ORR in alkaline fuel cells.

2. Experimental

2.1 Materials and reagents

Graphite powder and chitosan were purchased from Sinopharm Chemical Reagent Co., Ltd. Pt/C (20 wt%, Pt on Vulcan XC-72) was obtained from Alfa Aesar. Urea and boric acid were purchased from Beijing Chemical Company (China). Reagents including H_2SO_4 (98 %), $NaNO_3$, $KMnO_4$, H_2O_2 (30 %) and KOH were analytical grade and used without further purification. Distilled water was applied throughout the experiments.

2.2 Synthesis of Nitrogen-doped graphene aerogels (N-GAs)

GO was synthesized from graphite powder by following a modified Hummers' method.[30, 31] N-GAs was synthesized via a hydrothermal reaction of GO with urea and chitosan. The fabrication process for the N-GAs is demonstrated in Scheme 1. Briefly, GO was dispersed in deionized water by sonication, reaching a concentration up to 2.0 mg mL^{-1}. Afterwards, 50 mg chitosan and 1g urea were slowly added into 25 ml of the above dispersion. After constantly mechanical stirring for 10 min, a stable dark brown aqueous suspension was achieved (Scheme 1a). Subsequently, these quaternary components were sealed in a 50 mL Telfon-lined autoclave and hydrothermally treated at 180 ºC for 12 h to form 3D graphene-based hydrogels (Scheme 1b). After that, the vessel was allowed to return to room temperature. The as-prepared hydrogels were directly dehydrated via a freeze-drying process to maintain the 3D architecture

and then heated at 1000 °C for 2 h under argon. The heating rate is 10 ºC min^{-1}. The final fabricated product from this process is a black 3D hybrid of N-GAs (Scheme 1c). Simultaneously, graphene aerogels (GAs) was also prepared through the same steps as those used to make N-GAs without adding any urea in the ultrasonic vibration step.

2.3 Synthesis of Nitrogen, boron co-doped graphene aerogels (N, B-GAs)

The boron and nitrogen-dual-doped graphene aerogels were prepared via the pyrolysis of mixtures consisting of the pre-synthesized N-GAs (before pyrolysing) with H_3BO_3. N, B-GAs synthesis was carried out by putting N-GAs (~30 mg) above the H_3BO_3 (~30 mg) powder in an Al_2O_3 combustion boat. Then the samples were pyrolyzed at 800, 900 and 1000 ºC for 2 h in an Ar atmosphere, abbreviated as N, B-GAs-800, N, B-GAs-900 and N, B-GAs-1000, respectively. The heating rate is 10 ºC min^{-1}. After cooling to room temperature, the N, B-GAs was obtained. For comparison, boron single-doped graphene aerogels (B-GAs) were also prepared through the same steps as those used to make N, B-GAs with the addition of 30 mg GAs instead of N-GAs in the pyrolysis step.

2.4 Characterization

The morphology and structure of as-prepared samples were analyzed by scanning electron microscopy (SEM, JSM-6701F, operating at 5 kV) and transmission electron microscopy (TEM, JEOL-2010 transmission electron microscope operating at 200 kV). The crystalline phases of the resulting materials were analyzed by powder X-ray diffraction (XRD, RIGAK, D/MAX2550 VB/PC, Japan). X-ray photoelectron spectroscopy (XPS) measurements were carried out on an ESCLAB 250 spectrometer

using Al Kα as the exciting source (1486.6 eV photons) to identify the surface chemical composition and bonding state. Raman spectra were taken on a TriVista^{TM}555CRS Raman spectrometer at 785 nm. The Brunauer-Emmett-Teller (BET) surface area and pore volume were evaluated by using nitrogen adsorption-desorption isotherms measured on an ASAP2020 volumetric adsorption analyzer at 77 K.

2.5 Preparation of modified electrode and electrochemical measurements

Prior to modification, the working electrode was polished successively with 1.0, 0.3 and 0.05 mm aluminum oxide slurry, then thoroughly rinsed with distilled water, absolute ethanol and distilled water in turn for 1 min. Following, the cleaned GC electrode was blow-dried with N_2 at ambient temperature. Afterwards, a certain amount of ethanol suspension of N, B-GAs (1 mg mL^{-1}) was pipetted onto GC electrode and the coated electrode was then left to air dry. After evaporation of ethanol, 2 μL of a diluted Nafion solution (5 wt% in ethanol) was put on the top of the modified film, and then dried in air to hold the attachment of the film to the electrode surface. The total catalyst loading on the GC electrode was calculated to be 0.212 mg cm^{-2}. For comparison, the same amount of N-GAs, B-GAs or Pt/C (20 wt%) catalyst was also loaded onto the GC electrode with the same procedure.

Electrochemical measurements including rotating disk electrode (RDE), rotating ring-disk electrode (RRDE) and current-time (*i*-*t*) chronoamperometric response measurements were accomplished by a computer-controlled potentiostat (CHI660E electrochemical workstation, CH Instrument, USA) with a three-electrode cell system,

in which the modified GC electrode with catalyst was employed as the working electrode, a platinum-wire electrode as the auxiliary electrode, a saturated calomel electrode (SCE) as the reference electrode. RDE (5 mm in diameter) and RRDE (5.61 mm in diameter) measurements for the ORR were conducted at a GC rotating-disk electrode in an O_2-saturated 0.1 M KOH solution with a scan rate of 10 mV s^{-1}. The collection efficiency of platinum ring is 37 %. All electrochemical measurements were performed 3 times to avoid any incidental error.

3. Results and discussion

3.1 Characterizations of N, B-GAs composite

The morphology and structure of the as-prepared samples were characterized by means of scanning electron microscope (SEM) and transmission electron microscope (TEM). As displayed in Fig. 1a and b, N, B-GAs-1000 has a 3D interconnected framework of ultrathin graphene nanosheets with porous architecture. The partially crinkled nature may spring from the defective structures formed during the fabrication of GO and the heteroatom doping process.[32] The morphologies of the N-GAs, B-GAs, N, B-GAs-800 and N, B-GAs-900 are all similar to that of N, B-GAs-1000 (Fig. S1). Transmission electron microscopy (TEM) images disclose that the N, B-GAs-1000 displays a crumpled, cross-linked structure (Fig. 1c). The surface wrinkling and folding also generate lots of open edge sites, which were demonstrated to be favorable for sensing and electrocatalytic applications.[33, 34] The selected-area electron diffraction (SAED) pattern (inset in Figure 1c) shows that the diffraction ring is consistent with the typical hexagonal pattern of graphene with poor crystallinity.[14] The high-resolution TEM (HRTEM) image confirms that these layers show a layer

distance of about 0.34 nm (Fig. 1d), which is consistent with the separation of (002) layers of hexagonal graphite. The Brunauer- Emmett-Teller (BET) surface area and Barrett-Joyner-Halenda (BJH) pore size distribution of the different samples are characterized by nitrogen adsorption-desorption isotherms, as displayed in Fig. 1e and Fig. S2. These samples exhibit an IV hysteresis loop. The hysteresis loops appeared at lower (0.4-0.8) and higher (0.8-1.0) relative pressures, indicate the existence of mesopores and macropores, respectively. The BET surface area, BJH pore sizes, and pore volumes were summarized in Table 1. It is seen from Table 1, the BET specific surface area of N, B-GAs-1000 is 545.7 $m^2 \cdot g^{-1}$, which is much higher than that of B-GAs (100.1 m^2 g^{-1}) and N-GAs (141.5 m^2 g^{-1}). These results demonstrate that co-doping of nitrogen and boron elements facilitated the formation of large specific surface area during the pyrolysis process.

As shown in Fig. 2, the SEM and the corresponding elemental mapping images reveal that the N, B-GAs-1000 sample consists of C, N, O, and B, and the N and B elements in the graphene structure are distributed evenly, suggesting that nitrogen and boron were all doped in the graphene successfully. This result was further confirmed by the XPS analysis.

X-ray photoelectron spectroscopy (XPS) is a powerful tool to characterize the doping levels of heteroatoms. In the wide scan spectra (Fig. 3a), the peaks at around 400.0 and 192.0 eV refer to the nitrogen and boron atoms, respectively,[27] testifying successful incorporation of N and B into graphene upon annealing. The C1s peak and O1s peak are centered at about 284.8 and 532.7 eV, respectively. As expected, the

XPS survey spectra for N-GAs and B-GAs only show the N 1s and B 1s peak, respectively, while the corresponding XPS spectrum for N, B-GAs reveals both N 1s and B 1s peaks (Fig. 3a). The high-resolution XPS C 1s spectrum of N, B-GAs is given in Fig. 3b. Similar to the XPS spectra of vertically aligned BCN nanotubes,[35] the C 1s peak can be resolved into three components at 282.4 eV, 284.6 eV and 285.7 eV, attributable to the C–B, C–C and C–N bonds, respectively. The XPS spectra of N1s (Fig. 3c) and B1s (Fig. 3d) exhibit the local chemical binding state and relative contents of nitrogen and boron on the N, B-GAs. The XPS N1s spectrum of N, B-GAs-1000 can be deconvoluted into three peaks. The peaks at 398.6, 399.3 and 401.1 eV are attributed to pyridinic nitrogen, pyrrole nitrogen and graphitic nitrogen (or N-C-), respectively, [23, 36-38] without any N–B configuration (BE (binding energy) = 397.9 eV [12, 20]). The B1s XPS spectrum (Fig. 3d) can be deconvoluted into BC_3 (BE = 190.1 eV), B-C-O (including BC_2O and BCO_2, BE = 191.6 eV), and B-O (BE = 192.7 eV) moieties.[1] As a result, the structure of B-C-N hetero-rings is very likely to exist in N, B-GAs-1000. This is because its major components, B-C and C-N bonds, have already been justified in the XPS spectra while N-B bonds cannot be observed in the N1s spectrum. However, due to the complicated surface chemical states of the dopants, it is hard to exactly determine the binding energy and distinguish it from different moieties with similar binding energy values.[1] Remarkably, the area of these peaks significantly changes with increasing pyrolysis temperature, which suggests that different amounts of C, N and B bonding configurations were formed during pyrolysing at various temperatures. Fig. S3b, d and f graph the percentages of

different C, N and B species in the sample versus pyrolysis temperature. With increasing pyrolysis temperature from 800 to 1000 ºC, C-B and C-N bonds become dominant, while the content of C-C bond decreases (Fig. S3a and b). When the pyrolysis temperature is between 800 and 1000 ºC, the total content of N in N, B-GAs remains relatively unchanged. Furthermore, with the increase of pyrolysis temperature from 800 to 1000 ºC, pyridinic-N and graphitic-N become dominant, while the content of pyrrolic-N becomes lower (Fig. S3c and d). The results imply that high pyrolysis temperature does faintly influence the total content of nitrogen, but it can promote the formation of graphitic-N, pyridinic-N and prohibit the generation of pyrrolic-N, which is beneficial for nitrogen to form high-efficient active sites for the ORR.[39-41] It is seen from Fig. S3e and f, the content of boron atoms increases significantly with increasing the pyrolysis temperature from 800 to 1000 ºC and the content of BC_3 increases with the increase of pyrolysis temperature, which is operative for the ORR.[12] The above-mentioned results suggest that high pyrolysis temperature is beneficial for carbon, nitrogen and boron to form high-effective active sites for the ORR.

Raman spectra in Fig. 4a also provide information to study the structure of the final product. The two remarkable peaks around 1340 and 1580 cm^{-1} refer to the D band and G band of the graphene domain, respectively.[42] D band is related to the sp^3carbon at defective sites while G band corresponds to the E_{2g} stretching vibration mode of sp^2 carbon.[43] As shown in Fig. 3a, D and G bands emerge in all of the prepared catalysts. The increased D/G peak intensity ratio (I_D/I_G) of N, B-GAs-1000

(1.33 *vs*. 1.26 of N, B-GAs-900, 1.25 of N, B-GAs-800 and 1.10 of N-GAs) may suggest an increase in structural defects.[44] Fig. 4b shows the XRD patterns of GO, GAs and N, B-GAs-1000. The interlayer spacing of GO calculated from the XRD result is 8.7 Å, indicating the successful oxidization of graphite.[20] Moreover, the XRD patterns of both GAs and N, B-GAs-1000 exhibit strong diffraction peaks at 2θ = 25.1°and 26.3°, which can be attributed to the (002) lattice plane of the graphene sheets.[27] Based on these results, the thicknesses of N, B-GAs-1000 layer is found to be around 0.34 nm, the calculated results coincide well with the observed results by TEM.

3.2 Catalysis of the N, B-GAs hybrid for ORR

The CV measurements were performed to make better comparison among catalysts. Fig. 5 displays CVs of B-GAs, N-GAs, N,B-GAs-800, N,B-GAs-900, N,B-GAs-1000 and Pt/C in N_2- or O_2-saturated 0.1 M KOH at a scan rate of 100 mV s^{-1}. As shown in Fig. 5, featureless voltammetric current on N, B-GAs-1000 can be observed within the potential range of -0.8 to +0.2 V *vs.* SCE in a N_2-saturated 0.1 M KOH solution. After the solution was saturated with O_2, there is a conspicuous peak appeared at around -0.23 V *vs.* SCE for the ORR, which is ~0.03 and 0.06 V more positive than those of N, B-GAs-900 and N, B-GAs-800, respectively. This value is much more positive than that of B-GAs (-0.35 V *vs.* SCE) and N-GAs (-0.33 V *vs.* SCE), and the peak current increases obviously with increasing pyrolysis temperature. N, B-GAs-1000 displays more positive peak potential and the maximum peak current. These results suggest pyrolysis temperature can remarkably influence the

electrochemical catalytic activity of obtained N, B-GAs catalysts for the ORR.

The electrocatalytic activity of as-prepared catalysts toward the ORR was examined by linear sweep voltammetry (LSV). Fig. S4 shows LSV curves of N, B-GAs-1000 in N_2- or O_2-saturated 0.1 M KOH at the rotation speed of 1600 rpm with the scan rate of 10 mV s^{-1}. The cathodic current with the onset potential of -0.07 V *vs*. SCE is well-defined in an O_2-saturated 0.1 M KOH electrolyte. However, it is featureless in N_2-saturated 0.1 M KOH. Polarization curves of N, B-GAs-1000 and Pt/C were obtained at different rotation speeds with the scan rate of 10 mV s^{-1} (Fig. 6a and c). Fig. 6b and d display corresponding Koutecky-Levich (K-L) plots of N, B-GAs-1000 and Pt/C with the inverse current density (j^{-1}) versus the inverse of the square root of the rotation speed ($\omega^{-1/2}$) at different potentials. LSV curves and corresponding K-L plots of N-GAs, B-GAs, N, B-GAs-800 and N, B-GAs-900 were also obtained (see supplementary Fig. S5). The linearity of K-L plots and the near parallelism of fitting lines indicate the first-order reaction kinetics toward the concentration of the dissolved oxygen and the similar electron transfer number for the ORR at different potentials.[45, 46] Based on the slopes of K-L plots, the electron transfer number (n) was calculated as ~3.0, ~3.3, ~3.5, ~3.7, ~3.9 and ~4.0 at -0.4 − -0.7 V *vs*. SCE for B-GAs, N-GAs, N, B-GAs-800, N, B-GAs-900, N, B-GAs-1000 and Pt/C, respectively (Fig. 6e), indicating a four-electron process for the ORR on the N, B-GAs-1000 electrode. As can be seen in Fig. 6f, the onset potential of the N, B-GAs-1000 electrode for the ORR is at approximately ~ -0.07 V, which is more positive than those of the N-GAs electrode (~ -0.14 V) and the B-GAs electrode (~

-0.14 V). Besides, the diffusion current density from the N, B-GAs-1000 electrode is also much higher than those of the N-GAs and B-GAs electrodes, which is ascribed to the synergistic coupling of N and B. In addition, for the N, B-GAs pyrolyzed at different temperatures, the N, B-GAs-1000 displays more positive peak potential and the maximum peak current (Fig. 6f), which suggests pyrolysis temperature can also remarkably influence the electrocatalytic activity of obtained N, B-GAs catalysts for the ORR. The N, B-GAs-1000 electrocatalyst possesses the highest electrocatalytic activity towards the ORR among all graphene aerogels electrodes studied in the present work. Although the onset potential for the N, B-GAs-1000 electrode (~ -0.07 V) is still more negative than that for the Pt/C electrode (~ -0.02 V), the N, B-GAs-1000 electrode exhibits a higher oxygen reduction current density with respect to the Pt/C.

Tafel plots of LSVs are derived and shown in Supplementary Fig. S6. In order to evaluate the catalytic efficiency comprehensively, some electrochemical parameters for the ORR on these catalysts are compared according to polarization curves (see Supplementary Table S1). The excellent ORR activity of the N, B-GAs-1000 catalyst are also deduced from the much smaller Tafel slope (73 mV dec^{-1}) in the low overpotential region than those measured with B-GAs, N-GAs, N, B-GAs-800 and N, B-GAs-900 (Supplementary Table S1). The Tafel slope of 73 mV dec^{-1} is close to that of Pt/C (62 mV dec^{-1}), indicating that the ORR on these two catalysts has a similar catalytic mechanism.[47]

The electrocatalytic activity of our N, B-GAs-1000 catalyst is also compared

with those previously reported in literature (Table 2). It is worth noting that the onset potential, half-wave potential and limiting current density of our catalyst are comparable to or even better than those of previous reports (as shown in Table 2).

By using the rotating-ring-disk electrode (RRDE) technique, the H_2O_2 yield can be accurately determined from the disk and ring currents during the ORR. As shown in Fig. 7, the detected H_2O_2 yield for the N, B-GAs-1000 is below 10 % at a potential range of -0.3 to -0.7 V (vs. SCE) and corresponds to a high electron-transfer number of about 3.87, indicating a four-electron pathway reduction of O_2 on the N, B-GAs-1000, while H_2O_2 yields for the 3D B-GAs, 3D N-GAs , 3D N, B-GAs-800 and N, B-GAs-900 are as high as 50 %, 42%, 25 % and 13%, respectively (Fig. 7b). The calculated electron transfer number is about ~3.0, ~3.2, ~3.5 and ~3.8 for B-GAs, N-GAs, N, B-GAs-800 and N, B-GAs-900 (Fig. 7c). RRDE tests agree well with our results calculated from the Koutecky-Levich equation that the ORR electron transfer number for N, B-GAs-1000 is close to 4, further suggesting the ORR process on the N, B-GAs-1000 catalyst proceeds preferentially *via* a $4e^-$ pathway.

The crossover of fuel molecules (e.g. methanol) from the anode to the cathode in a fuel cell not only lowers the operation voltage due to the generation of mixed potential but also deteriorates the catalytic activity of Pt catalysts.[4, 48] The methanol crossover effect was evaluated using chronoamperometric measurements at -0.3 V in O_2-saturated 0.1 M KOH at a rotation rate of 1600 rpm with the addition of 3.0 M methanol (Fig. 8a). A significant drop in current appears at the Pt/C electrode upon the addition of 3.0 M methanol. In contrast, no noticeable change is observed in the ORR

current at the N, B-GAs-1000 electrode. This suggests that the N, B-GAs-1000 electrode has a higher ORR selectivity and greater tolerance to methanol crossover than the commercial Pt/C catalyst. Additionally, chronoamperometric durability tests for the ORR were also performed (Fig. 8b). It can be seen that the current for the ORR at the Pt/C electrode is only about 80% of the initial current after 10000 s, while the N, B-GAs-1000 electrode experiences only less than 5% loss in the reduction current, clearly indicating that the latter has much better stability than the former in an alkaline environment.

The activity enhancement of N, B-GAs-1000 for the ORR suggests that our fabricated catalyst is beneficial for energy generation. In the first place, the N, B-GAs-1000 catalyst possesses the large specific surface area, 3D interconnected framework and intriguing properties of graphene, thus providing favorable reaction spaces and facilitating the electron transport [2, 18, 49]. In the meantime, the structure of our N, B-GAs-1000 catalyst with macro/mesoporosity ensures the accessible porosity and effective mass transport [23, 49, 50]. Besides, N, B-GAs-1000 not only has relatively high nitrogen content and the highest boron content, but also possesses dominating active nitrogen (pyridinic nitrogen and graphitic nitrogen) and boron (BC_3), which is operative for the ORR.[12] More importantly, the synergistic effect of heteroatoms (N and B) among graphene framework conduces to enhance the catalytic activity markedly for the ORR.

4. Conclusions

We have proposed a two-step method to prepare N and B co-doped graphene aerogels as an effective metal-free ORR catalyst. The synthesis involved a hydrothermal reaction of GO with urea and chitosan to prepare N-GAs and an annealing step of the mixture of N-GAs and boric acid to give N, B-GAs. The final N, B-GAs-1000 exhibited excellent ORR performance due to the synergistic improvement effect between N and B. The N, B co-doped catalyst showed excellent methanol tolerance and improved durability, which is superior to the commercial Pt/C catalyst. Compared with other synthetic methods, our approach requires only common chemicals and nontoxic precursors, is thus environmental friendly. The high performance and excellent stability of N, B-GAs-1000 makes it a promising catalyst for the ORR in alkaline fuel cells.

Acknowledgements

This research has been financed by the National Natural Science Foundation of China (No. 21273024).

References

1. J. Tai, J. T. Hu, Z. X. Chen and H. B. Lu, *RSC Adv*., 2014, **4**, 61437–61443.
2. Z. S. Wu, S. B. Yang, Y. Sun, K. Parvez, X. L. Feng, and K. Müllen, *J. Am. Chem. Soc*., 2012, **134**, 9082−9085.
3. T. C. Zhou, J. Zhang, J. L. Qiao, L. L. Liu, G. P. Jiang, J. Zhang, Y. Y. Liu, *J. Power Sources*, 2013, **227**, 291-299.
4. J. T. Zhang, C. X. Guo, L. Y. Zhang and C. M. Li, *Chem. Commun*., 2013, **49**,

6334-6336.

5. L. Zhang, J. J. Zhang, D. P. Wilkinson, H. J. Wang, *J. Power Sources*, 2006, **156**, 171–182.
6. R. Z. Zhang, S. J. He, Y. Z. Lu and W. Chen, *J. Mater. Chem. A*, 2015, **3**, 3559–3567.
7. Y. H. Su, H. L. Jiang, Y. H. Zhu, X. L. Yang, J. H. Shen, W. J. Zou, J. D. Chen and C. Z. Li, *J. Mater. Chem. A*, 2014, **2**, 7281–7287.
8. D. D. Wang, X. Chen, D. G. Evans and W. S. Yang, *Nanoscale*, 2013, **5**, 5312–5315.
9. Z. Y. Wu, P. Chen, Q. S. Wu, L. F. Yang, Z. Pan and Q. Wang, *Nano Energy*, 2014, **8**, 118–125.
10. Z. Yao, H. G. Nie, Z. Yang, X. M. Zhou, Z. Liu and S. M. Huang, *Chem. Commun*., 2012, **48**, 1027–1029.
11. G. Elumalai, H.Noguchia and K. Uosaki, *Phys. Chem. Chem. Phys*., 2014, **16**, 13755-13761.
12. Y. Zheng, Y. Jiao, L. Ge, M. Jaroniec, and S. Z. Qiao, *Angew. Chem. Int. Ed*., 2013, **52**, 3110–3116.
13. Z. H. Sheng, H. L. Gao, W. J. Bao, F. B. Wang and X. H. Xia, *J. Mater. Chem*., 2012, **22**, 390–395.
14. J. T. Jin, F. P. Pan, L. H. Jiang, X. G. Fu, A. M. Liang, Z. Y. Wei, J. Y. Zhang, and G. Q. Sun, *ACS nano*, 2014, **8**, 3313–3321.
15. Y. J. Gong, H. L. Fei, X. L. Zou, W. Zhou, S. B. Yang, G. L. Ye, Z. Liu, Z. W.

Peng, J. Lou, R. Vajtai, B. I. Yakobson, J. M. Tour, and P. M. Ajayan, *Chem. Mater*., 2015, **27**, 1181−1186.

16. P. Chen, L. K. Wang, G. Wang, M. R. Gao, J. Ge, W. J. Yuan, Y. H. Shen, A. J. Xie and S. H. Yu, *Energy Environ. Sci*., 2014, **7**, 4095–4103.
17. P. Chen, T. Y. Xiao, Y. H. Qian, S. S. Li and S. H. Yu, *Adv. Mater*., 2013, **25**, 3192–3196.
18. Y. R. Li, J. Chen, L. Huang, C. Li, J. D. Hong, and G. Q. Shi, *Adv. Mater*., 2014, **26**, 4789–4793.
19. S. Y. Zhao, J. Liu, C. X. Li, W. B. Ji, M. M. Yang, H. Huang, Y.Liu, and Z. H. Kang, *ACS Appl. Mater. Interfaces*, 2014, **6**, 22297−22304.
20. C. H. Choi, M. W. Chung, H. C. Kwon, S. H. Park and S. I. Woo, *J. Mater. Chem. A*, 2013, **1**, 3694–3699.
21. J. E. Park, Y. J. Jang, Y. J. Kim, M. S. Song, S. Yoon, D. H. Kim and S. J. Kim, *Phys. Chem. Chem. Phys*., 2014, **16**, 103-109.
22. L. Xu, G. S Pan and X. L. Liang, *RSC Adv*., 2014, **4**, 19756–19765.
23. Y. H. Xue, D. S. Yu, L. M. Dai, R. G. Wang, D. Q. Li, A. Roy, F. Lu, H. Chen, Y. Liu and J. Qu, *Phys. Chem. Chem. Phys*., 2013, **15**, 12220-12226.
24. E. Iyyamperumal, S. Y. Wang, and L. M. Dai, *ACS nano*, 2012, **6**, 5259–5265.
25. C. K. Chang, S. Kataria, C. C. Kuo, A. Ganguly, B. Y. Wang, J. Y. Hwang, K. J. Huang, W. H. Yang, S. B. Wang, C. H. Chuang, M. Chen, C. I Huang, W. F. Pong, K. J. Song, S. J. Chang, J. H. Guo, Y. Tai, M. Tsujimoto, S. Isoda, C. W. Chen, L. C. Chen and K. H. Chen, *ACS nano*, 2013, **7**, 1333–1341.

26. D. C. Wei, L. Peng, M. L. Li, H. Y. Mao, T. C. Niu, C. Han, W. Chen and A. T. S. Wee, *ACS nano*, 2015, **9**, 164–171.

27. J. L. Zhu, C. Y. He, Y. Y. Li, S. Kang and P. K. Shen, *J. Mater. Chem. A*, 2013, **1**, 14700–14705.

28. Z. J. Wang, X. H. Cao, J. F. Ping, Y. X. Wang, T. T. Lin, X. Huang, Q. L. Ma, F. K. Wang, C. B. He and H. Zhang, *Nanoscale*, 2015, **7**, 9394–9398.

29. D. H. Deng, X. L. Pan, L. Yu, Y. Cui, Y. P. Jiang, J. Qi, W. X. Li, Q. Fu, X. C. Ma, Q. K. Xue, G. Q. Sun and X. H. Bao, *Chem. Mater*., 2011, **23**, 1188–1193.

30. Y.X. Xu, L. Zhao, H. Bai, W.J. Hong, C. Li, G.Q. Shi, *J. Am. Chem. Soc*., 2009, **131**, 13490.

31. W. S. Hummers and R. E. Offeman, *J. Am. Chem. Soc*., 1958, **80**, 1339.

32. S. B. Yang, L. J. Zhi, K. Tang, X. L. Feng, J. Maier and K. Müllen, *Adv. Funct. Mater*., 2012, **22**, 3634–3640.

33. X. J. Zhou, Z. Y. Bai, M. J. Wu, J. L. Qiao and Z. W. Chen, *J. Mater. Chem. A,* 2015, **3**, 3343–3350.

34. L. Chen, R. Du, J. H. Zhu, Y. Y. Mao, C. Xue, N. Zhang, Y. L. Hou, J. Zhang and T. Yi, *Small*, 2015, **11**, 1423–1429.

35. S. Y. Wang, E. Iyyamperumal, A. Roy, Y. H. Xue, D. S. Yu and L. M. Dai, *Angew. Chem., Int. Ed*., 2011, **50**, 11756–11760.

36. S. Z. Li, Y. Y. Hu, Q. Xu, J. Sun, B. Hou, Y. P. Zhang, *J. Power Sources*, 2012, **213**, 265–269.

37. K. Y. Kang, B. I. Lee, J. S. Lee, *Carbon*, 2009, **47**, 1171–1180.

38. J. I. Ozaki, T. Anahara, N. Kimura, A. Oya, *Carbon,* 2006, **44**, 3348–3378.

39. M. Vikkisk, I. Kruusenberg, U. Joost, E. Shulga, I. Kink and K. Tammeveski, *Appl. Catal*., 2014, **147**, 369–376.

40. B. Zhang, Z. Wen, S. Ci, S. Mao, J. Chen, Z. He, *ACS Appl. Mater. Interfaces*, 2014, **6**, 7464–7470.

41. L. Lai, J. R. Potts, D. Zhan, L. Wang, C. K. Poh, C. Tang, H. Gong, Z. Shen, J. Lin, R. S. Ruoff, *Energy Environ. Sci*., 2012, **5**, 7936–7942.

42. C. H. Choi, S. H. Park and S. I. Woo, *ACS nano*, 2012, **6**, 7084-7091.

43. Y. A. Kim, K. Fujisawa, H. Muramatsu, T. Hayashi, M. Endo, T. Fujimori, K. Kaneko, M. Terrones, J. Behrends, A. Eckmann, C. Casiraghi, K. S. Novoselov, R. Saito and M. S. Dresselhaus, *ACS nano*, 2012, **6**, 6293-6300.

44. Z. Mo, R. Zheng, H. Peng, H. Liang and S. Liao, *J. Power Sources*, 2014, **245**, 801-807.

45. K. J. J. Mayrhofer, D. Strmcnik, B. B. Blizanac, V. Stamenkovic, M. Arenz, N. M. Markovic, *Electrochim. Acta,* 2008, **53**, 3181-3188.

46. H. L. Fei, R. Q. Ye, G. L. Ye, Y. J. Gong, Z. W. Peng, X. J. Fan, E. L. G. Samuel, P. M. Ajayan and J. M. Tour, *ACS nano*, 2014, **8**, 10837-10843.

47. S. K. Bikkarolla, F. J. Yu, W. Z. Zhou, P. Joseph, P. Cumpson, P. Papakonstantinou, *J. Mater. Chem. A,* 2014, **2**, 14493-14501.

48. Y. H. Su, H. L. Jiang, Y. H. Zhu, X. L. Yang, J. H. Shen, W. J. Zou, J. D. Chen and C. Z. Li, *J. Mater. Chem. A*, 2014, **2**, 7281-7287.

49. Z. H. Zhang and P. Y. Wu, *RSC Adv*., 2014, **4**, 45619–45624.

50. C. Z. Zhu and S. J. Dong, *Nanoscale*, 2013, **5**, 1753–1767.

Figure captions

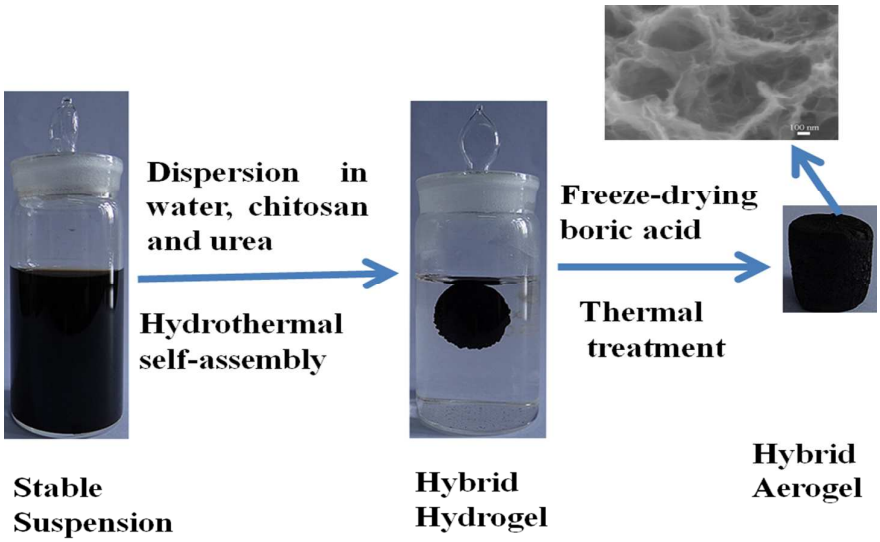

Scheme. 1 Schematic illustration of preparation of N, B-GAs. (a) Stable suspension of GO, chitosan, and urea dispersed in a vial. (b) 3D hybrid hydrogels of N, B-GAs formed via hydrothermal self-assembly process. (c) A bulk aerogels of N, B-GAs obtained after freeze-drying process and thermal treatment.

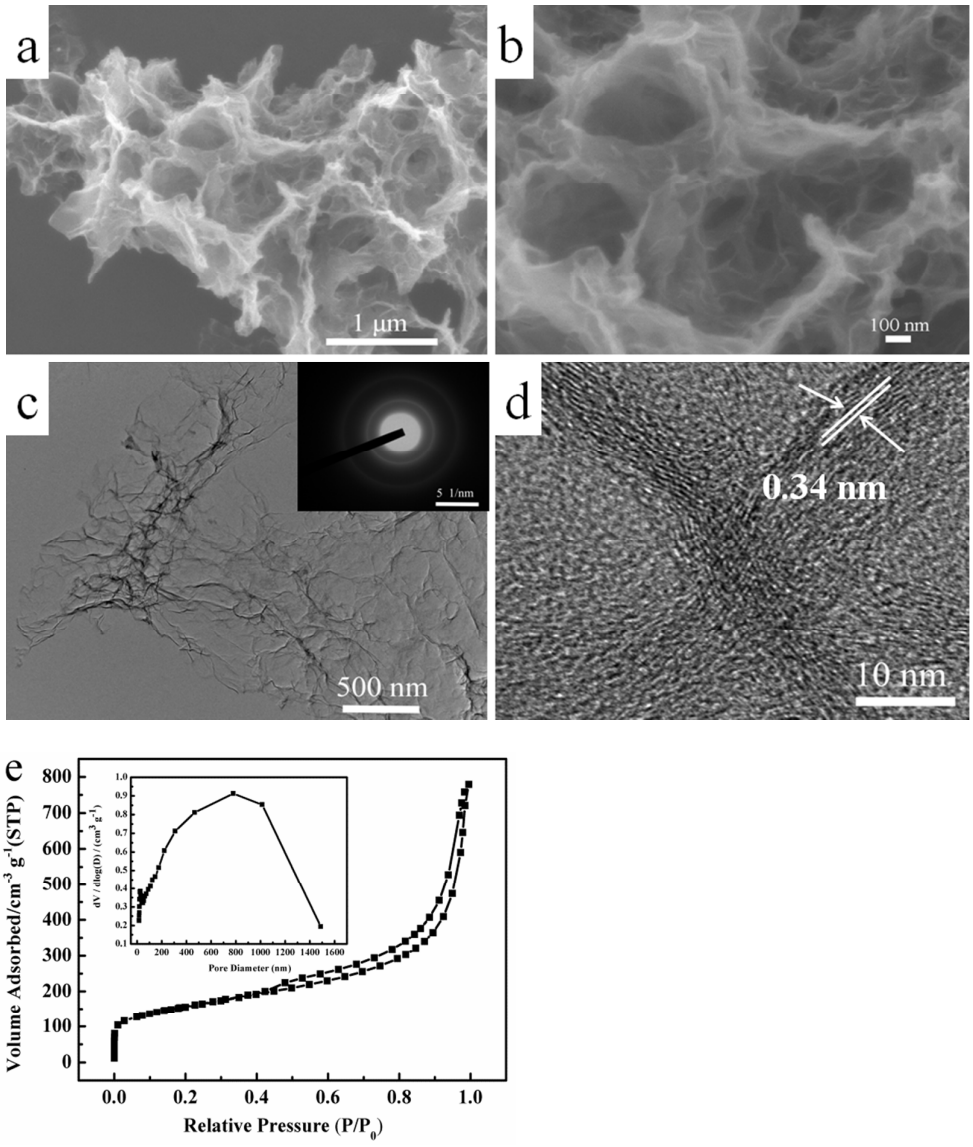

Fig. 1 (a, b) SEM images of N, B-GAs-1000 at different magnifications. (c) TEM images of N, B-GAs-1000. The inset shows the corresponding selected-area electron diffraction pattern. (d) HRTEM image of N, B-GAs-1000. (e) Nitrogen adsorption-desorption isotherms. The inset is the pore size distribution of N, B-GAs-1000 gained by the Barrett-Joyner-Halenda method.

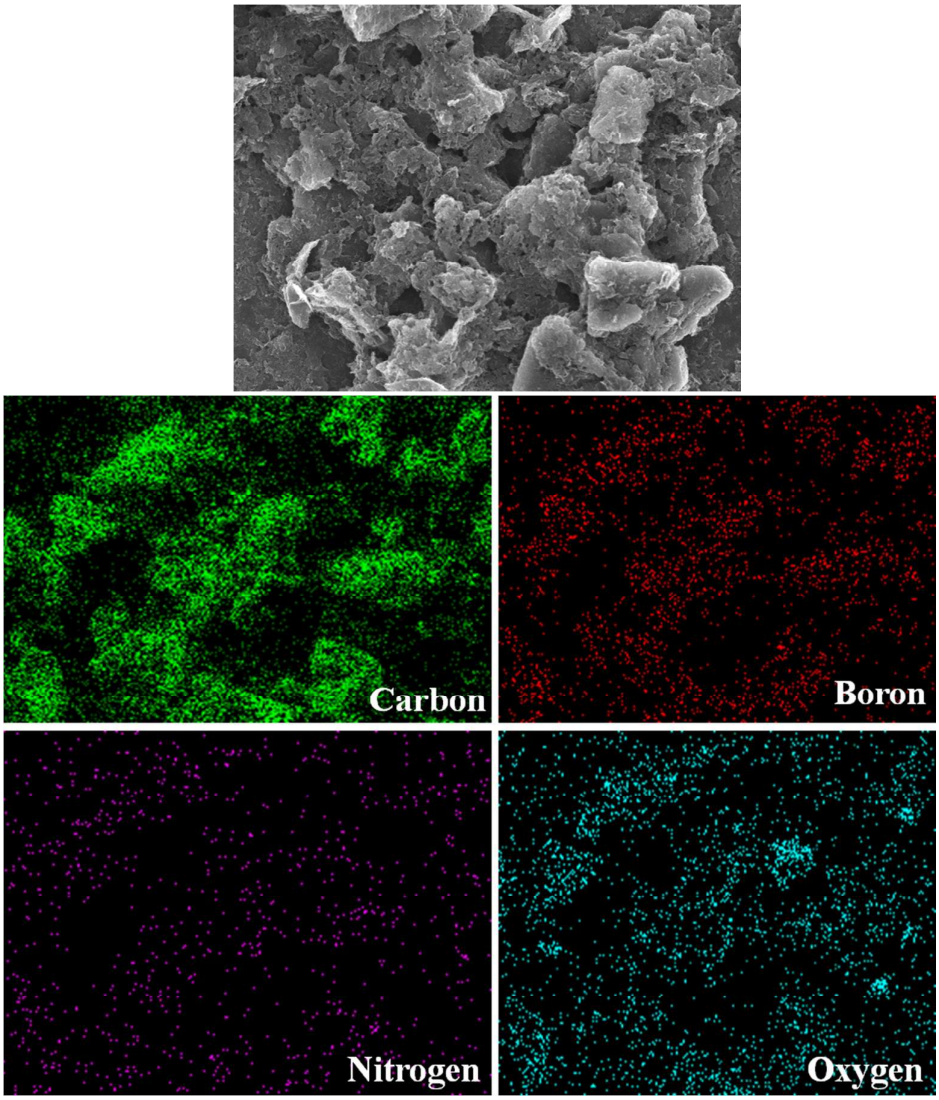

Fig. 2 SEM image of N, B-GAs-1000 and the corresponding EDS mapping of C, B, N and O elements.

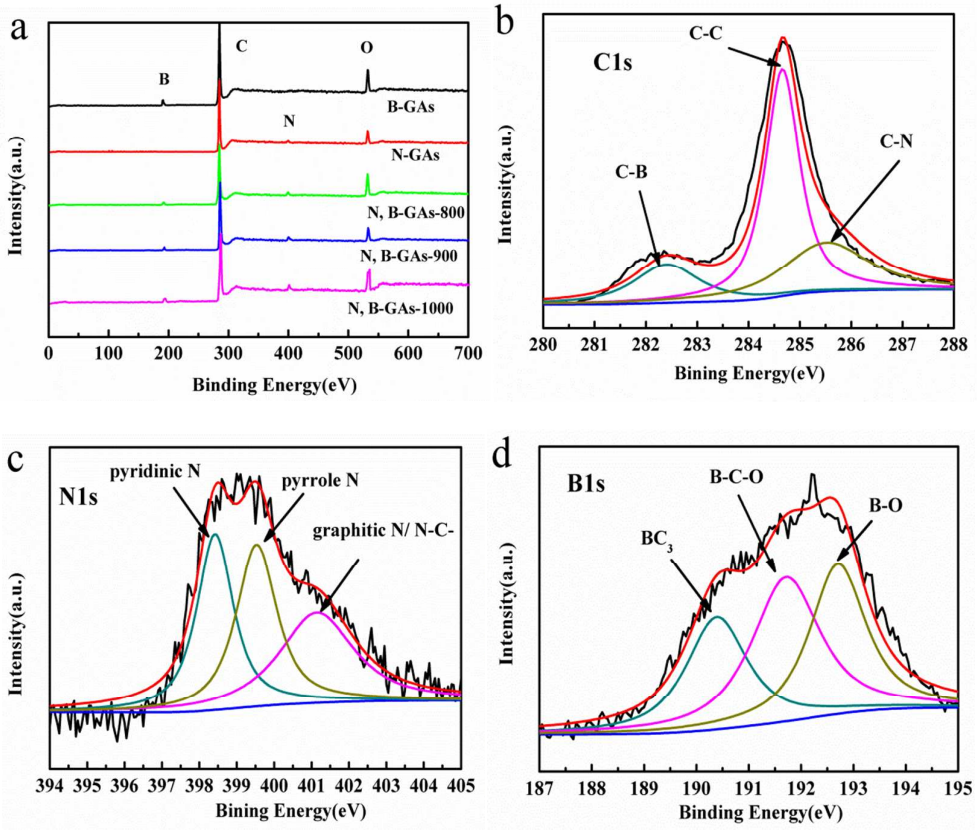

Fig. 3 (a) XPS survey spectra of B-GAs, N-GAs, N, B-GAs-800, N, B-GAs-900 and N, B-GAs-1000. (b) High resolution C1s spectra of N, B-GAs-1000. (c) High resolution N1s spectra of N, B-GAs-1000. (d) High resolution B1s spectrum of N, B-GAs-1000.

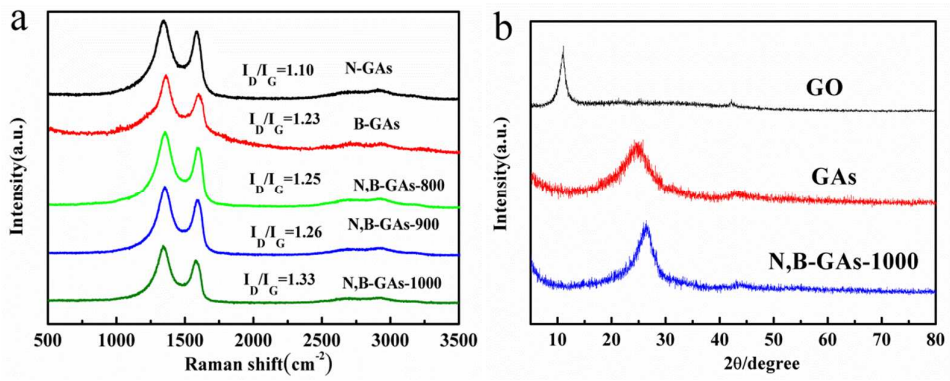

Fig. 4 (a) Raman spectra and (b) XRD patterns of different samples.

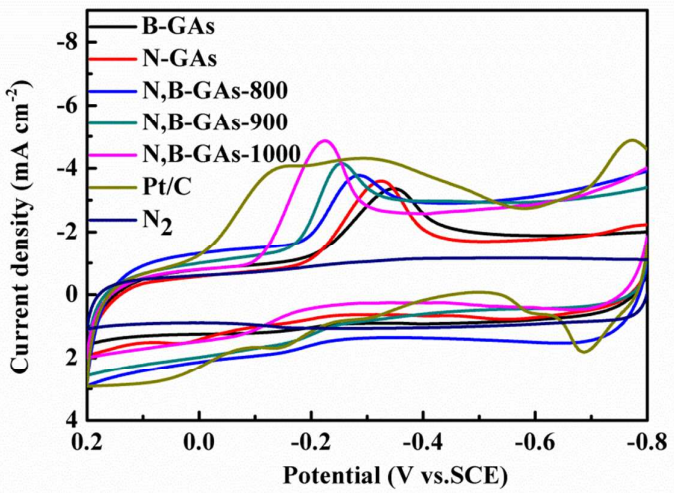

Fig. 5 CVs of N,B-GAs-1000 in N_2- or O_2- saturated 0.1 M KOH at a scan rate of 100 mV $s^{-1}$and CVs of B-GAs, N-GAs, N,B-GAs-800, N,B-GAs-900 and Pt/C in O_2-saturated 0.1 M KOH at a scan rate of 100 mV s^{-1}.

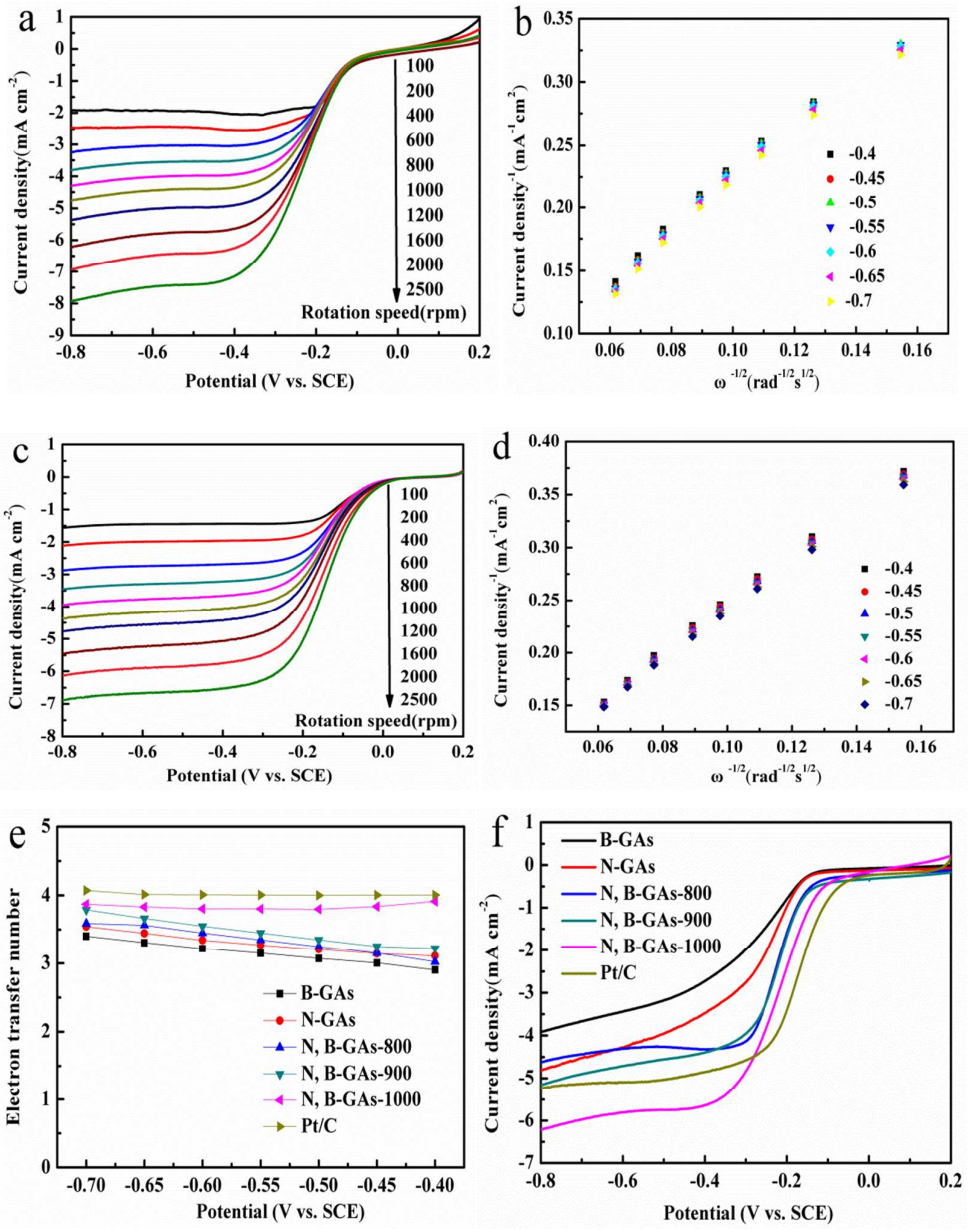

Fig. 6 (a, c) LSV curves of (a) N, B-GAs-1000 and (c) Pt/C at different rotation speeds in O_2-saturated 0.1M KOH with the scan rate of 10 mV s^{-1}. K-L plots of (b) N, B-GAs-1000 and (d) Pt/C at fixed potentials of -0.4, -0.45, -0.5, -0.55, -0.6, -0.65, -0.7 V *vs*. SCE. (e) The number of electrons transferred at different potentials for different samples. (f) LSV curves of different samples in O_2-saturated 0.1 M KOH at 1600 rpm with the scan rate of 10 mV s^{-1}.

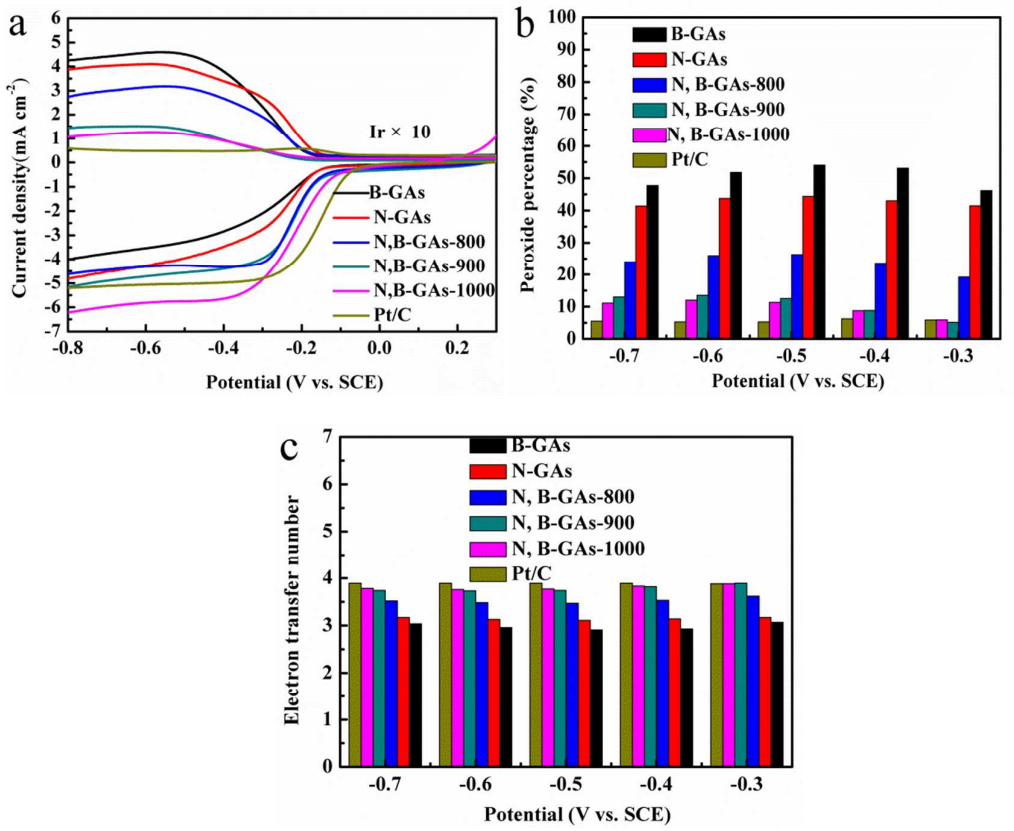

Fig. 7 (a) RRDE tests of the ORR on different samples in O_2-saturated 0.1 M KOH at the rotation speed of 1600 rpm with the scan rate of 10 mV s^{-1}. The Pt ring electrode is polarized at 0.6 V *vs*. SCE. (b) Peroxide percentage and (c) electron transfer number of different samples at various potentials, based on corresponding RRDE data in (a).

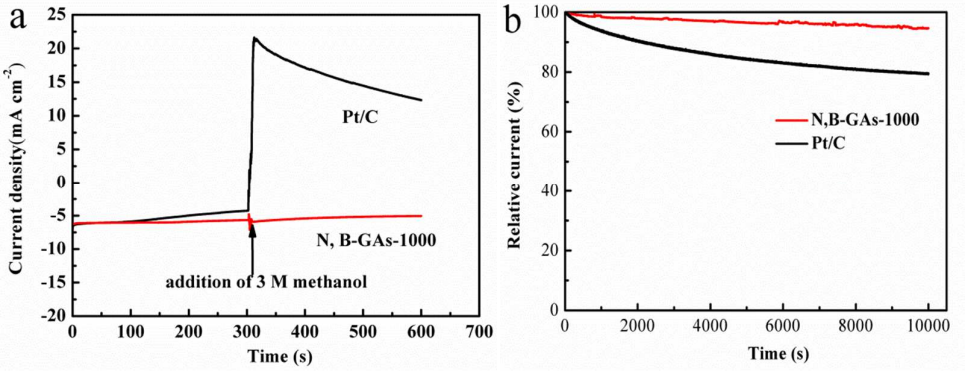

Fig. 8 (a) Current density–time chronoamperometric responses of Pt/C and N, B-GAs-1000 electrodes at -0.3 V with the rotating speed of 1600 rpm in oxygen-saturated 0.1 M KOH. The arrow indicates the addition of methanol into the electrolytic cell. (b) The durability of electrodes for ORR.

Table 1 Textural parameters of B-GAs, N-GAs and N, B-GAs-1000.

Sample	SA[a] (m^2 g^{-1})	PV[b] (cm^3 g^{-1})	PD[c] (nm)
B-GAs	100.1	0.47	185.6
N-GAs	141.5	0.56	137.5
N, B-GAs-1000	545.7	1.21	88.3

[a] BET surface area. [b] Pore volume. [c] Average pore size determined by BJH method.

Table 2 A bench mark of our N, B-GAs-1000 catalyst with values obtained from some other independent literatures. All in the alkaline condition with 0.1 M KOH.

Electrocalyst	ΔE_{onset} [a,c] (V)	$\Delta E_{1/2}$ [a,c] (V)	j_L [b,c] (mA cm^{-2})	The catalyst load ing per area (μg cm^{-2})	Reference electrode	Ref.
N, B-GAs-1000	-0.05	-0.04	6.2	212	SCE	In this work
BNG	-0.09	-0.11	5.5	100	Ag/AgCl	1
B,N-graphene	-0.12	-0.14	5.2 (1500 rpm)	280	Ag/AgCl	12
BCN-2.5-1000	-0.003	0.004	6.2	283	Ag/AgCl	14
BNC-2	0.1	0.09	3.5	Not mentioned	Ag/AgCl	15
N-doped GNR aerogels	0.01	-0.06	2.2	Not mentioned	Ag/AgCl	15
NPBC-2	-0.05	-0.11	3.5	100	SCE	19
BN-GF/GC	-0.15	-0.11	5.5	Not mentioned	SCE	23
BNG-1000	-0.04	0.03	4.4	606	RHE	27
NB-3DGN	-0.02	-0.07	6.0	Not mentioned	Ag/AgCl	28

a represents the difference of onset potentials or half-wave potentials between various catalysts and Pt/C.

b represents diffusion-limited current densities of various catalysts at the rotation speed of 1600 rpm.

c The onset potential (E_{onset}), half-wave potential ($E_{1/2}$) and diffusion-limited current density (j_L) are reported from the corresponding literatures and the corresponding figures in the present studies.